



**HAL**  
open science

## Elastic behavior of anisotropic coatings sputter-deposited at oblique incidence

Elia Zgheib, Akram Alhussein, Mohamed Fares Slim, Khaled Khalil, Manuel  
François

► **To cite this version:**

Elia Zgheib, Akram Alhussein, Mohamed Fares Slim, Khaled Khalil, Manuel François. Elastic behavior of anisotropic coatings sputter-deposited at oblique incidence. *International Journal of Mechanical Sciences*, 2020, pp.106050. 10.1016/j.ijmecsci.2020.106050 . hal-02927590

**HAL Id: hal-02927590**

**<https://utt.hal.science/hal-02927590>**

Submitted on 17 Oct 2022

**HAL** is a multi-disciplinary open access archive for the deposit and dissemination of scientific research documents, whether they are published or not. The documents may come from teaching and research institutions in France or abroad, or from public or private research centers.

L'archive ouverte pluridisciplinaire **HAL**, est destinée au dépôt et à la diffusion de documents scientifiques de niveau recherche, publiés ou non, émanant des établissements d'enseignement et de recherche français ou étrangers, des laboratoires publics ou privés.



Distributed under a Creative Commons Attribution - NonCommercial 4.0 International License

# Elastic behavior of anisotropic coatings sputter-deposited at oblique incidence

Elia Zgheib<sup>a,d,\*</sup>, Akram Alhussein<sup>a</sup>, Mohamed Fares Slim<sup>c</sup>, Khaled Khalil<sup>d</sup> and Manuel François<sup>b</sup>

<sup>a</sup> LASMIS-ICD, Université de Technologie de Troyes, Antenne de Nogent, Pôle Technologique Sud-Champagne, 52800, Nogent, France

<sup>b</sup> LASMIS-ICD, Université de Technologie de Troyes, 12 Rue Marie Curie, CS 42060, 10004, Troyes, France

<sup>c</sup> Institut Jean Lamour, Université de Lorraine, UMR 7198, CNRS, 54000, Nancy, France

<sup>d</sup> Lebanese University, Faculty of Engineering, CRSI, MGC, Equipe MMC, Tripoli, Lebanon

\* Corresponding author: Elia Zgheib, [elia.zgheib@utt.fr](mailto:elia.zgheib@utt.fr)

## Abstract

In this work, the elasticity constants of anisotropic thin films were determined using a model developed specifically in order to use the Impulse Excitation Technique (IET). The model is based on the lamination theory and was validated with a finite element analysis. The IET was used in flexural and torsional vibration modes in order to determine the Young's and shear moduli of coatings. The anisotropic behavior was evaluated for titanium thin films deposited by magnetron sputtering at Glancing Angle Deposition (GLAD) on glass substrates and silicon wafers. The elastic response was examined for three different glancing angles and the presence of in-plane anisotropy of the film was noticed from the measured elasticity constants. The difference between conventional and GLAD sputtering was evaluated in terms of microstructure, texture evolution and elastic properties. The influence of the film porosity on the elasticity constants was investigated. Nanoindentation measurements were performed in order to evaluate the effect of the glancing angle on the hardness and the reduced modulus. The results revealed that the elasticity constants of the titanium thin film were mostly affected by the glancing angle and they decreased when the glancing angle increased. The same effect was noticed for the film hardness and reduced modulus. Upon increasing the glancing angle, the film anisotropy was increased owing to different factors, among which the non-standard columnar growth and the inclined crystallites toward the vapor flux direction.

## Keywords

Elasticity constants, Titanium thin films, Magnetron sputtering, GLAD, Nanostructured films, Dynamical resonant method.

## 1. Introduction

Since the appearance of thin film technology, there has been a growing interest in using the film structure to control its physical properties. Several technological advances have been achieved in terms of surface morphology and film microstructure. Glancing angle deposition technique (GLAD), first reported more than a hundred years ago [1] has been one of the techniques employed to control the structure of thin films. This technique provides a simple method to design various nanostructured columnar architectures using prevalent processes such as sputtering or evaporation. The purpose of the GLAD process is to modify the substrate inclination in order to control ballistic shadowing and nanocrystallized film growth during deposition. The ballistic effect becomes a dominant effect in GLAD extending the total shadow lengths thanks to the oblique deposition geometry. A highly porous film microstructure is developed with directional column growth. Thanks to their dedicated porosity, texture and anisotropic properties, these nanostructured thin films have been used in optics [2], nanomechanics [3] and many other applications in order to enhance the performance of those components.

The GLAD process can be used under the stationary mode, where columns oriented towards the incoming vapor flux are formed. Along with the pressure, temperature, substrate bias voltage and the deposition rate, an important experimental parameter is used in GLAD to modify the film properties. This parameter is the direction of the incident flux of the deposited species with respect to the substrate surface. It is defined by the angle  $\alpha$  formed by the substrate normal and the target normal. **On the other hand**, the GLAD process can be used in dynamic mode by employing an additional substrate motion during glancing deposition. In this case, more complex film architectures like spiral, zigzag or nanorods structures can be obtained [4,5].

The determination of the mechanical properties of these structured thin films was mostly performed by NanoIndentation (NI) as a static technique. Among the works in the literature, we can cite those performed on  $\text{TiO}_2\text{-SiO}_2$  multilayers with different microstructures [6], on  $\text{TiO}_2$  thin films in inclined columns and zigzag multilayers [7], on  $\text{TiAlN}$  tilted columns [8], and on chromium zigzag multilayers [3]. The NI technique simply leads to an overall elastic modulus that depends on the elastic moduli in the three directions.

Regarding the elastic properties, several studies [9,10] used the resonant method to simultaneously measure the density and Young's modulus of thin films. This proposed method requires the use of a beam composed of three layers (substrate + film 1+ film 2) in

order to attribute one analytical expression for each film. Ma et al. [10] used this method to simultaneously measure the Young's modulus and density of Ni film deposited on Si cantilever beam.

Recently, it has been shown that Young's modulus and density of thin films can also be simultaneously determined by measuring the in-plane and out-of-plane resonant frequencies [11]. However, the in-plane excitation is difficult to achieve in practice. On the other hand, another non-destructive method was proposed to simultaneously determine the Young's modulus and either the density or the thickness of thin films [12]. It consists of detecting the resonant frequency shifts of coated and uncoated resonators caused by the attached mass. Using the well-established resonant based mass sensors, the film properties were determined even though no resonant frequency shift was detected.

To our knowledge, the determination of the anisotropic elasticity constants of nanostructured thin films seems inexistent in the literature. In this context, the objective of the present work is to propose a new methodology to determine the rigidity of anisotropic thin films deposited with the GLAD technique. This methodology is applied using the Impulse Excitation Technique (IET), which is a dynamic technique with a newly developed model that takes into account the anisotropy of these thin films based on the laminated theory. This theory was used previously to determine the Young's modulus of isotropic thin films [13-16]. In the first section, the development of the mechanical model is represented using analytical and numerical methods. Secondly, the deposition process of pure Ti films with different glancing angles is presented, followed by different structural and microstructural characterizations. The results of the elasticity constants of Ti thin films with their standard uncertainties are presented in the last section.

## 2. Modeling

### 2.1. Homogeneous beam

The flexural and torsional resonance equations of beams have been developed in order to determine the Young's and shear moduli of an isotropic material subjected to flexural and torsional vibrations. In the case of a free-free beam with rectangular cross-section, the Young's and shear moduli can be determined from the following equations [14,17]:

$$E_s = 0.9465 k F_s^2 \rho_s \frac{L^4}{h_s^2} \quad (1)$$

$$G_s = 4 R L^2 \rho_s T_s^2 \quad (2)$$

with:

$$k = 1 + 6.585 \left(\frac{h_s}{L}\right)^2 \quad (3)$$

$$R = \left[ \frac{1 + \left(\frac{b}{h_s}\right)^2}{4 - 2.521 \frac{h_s}{b} \left(1 - \frac{1.991}{e^{\frac{\pi b}{h_s}} + 1}\right)} \right] \left[ 1 + \frac{0.00851 b^2}{L^2} \right] - 0.06 \left(\frac{b}{L}\right)^{\frac{3}{2}} \left(\frac{b}{h_s} - 1\right)^2 \quad (4)$$

where:

$k$ : geometrical correction factor, used to take into account the shear and rotatory effects,

$R$ : dimensionless shape factor,

The index  $s$  refers to the substrate,

$E$ : Young's modulus,

$G$ : shear modulus,

$\nu$ : Poisson's ratio,

$L$ : length,

$b$ : width,

$h$ : thickness,

$\rho$ : density,

$F$ : first flexural resonance frequency,

$T$ : first torsional resonance frequency.

## 2.2. Coated substrate with isotropic behavior

In the literature, two theories were used to develop mechanical models able to determine the Young's modulus of isotropic thin films. The first model is the flexural rigidity of a composite beam and the second one is the classical laminated beam theory. The difference between the two theories was discussed in a recent study [18]. Several models were developed to determine the elasticity constants of isotropic film. Lopez's model [19] was developed to determine the film Young's modulus without considering the shift of the neutral axis after deposition. Berry's model [14] was used as a simplified approach, which can be obtained from the first-order Taylor series expansion of Lopez's model. Pautrot's et al. [19] modified Lopez's model by taking into account the shift of the neutral axis after deposition. For the determination of the shear modulus, Gadaud's model [20] has been developed based

on Hamilton's principle without taking into account the shift of the neutral axis after deposition. Slim et al. [17,21] developed an enhanced formulation to determine the shear modulus by considering the shift of the neutral axis after deposition.

By assuming an isotropic behavior, the Young's modulus of a thin film can be determined, based on the laminated theory, from the flexural resonance equation of a free-free composite beam (substrate + film) with rectangular cross-section, as follows [18]:

$$R_F = \frac{2}{h_s} \sqrt{\frac{3\rho_s}{E_s \rho_{eff} d_{11}}} \quad (5)$$

where:

$$R_F = \frac{F_t}{F_s} \quad (6)$$

$$\rho_{eff} = \rho_s h_s + \rho_c h_c \quad (7)$$

$$d_{11} = \frac{\frac{E_s R_s}{1 - \nu_s^2} + \frac{E_c R_c}{1 - \nu_c^2}}{\left[ \frac{E_s R_s}{1 - \nu_s^2} + \frac{E_c R_c}{1 - \nu_c^2} \right]^2 - \left[ \frac{\nu_s E_s R_s}{1 - \nu_s^2} + \frac{\nu_c E_c R_c}{1 - \nu_c^2} \right]^2} \quad (8)$$

$$R_s = \frac{h_s^3}{3} - e h_s^2 + e^2 h_s \quad (9)$$

$$R_c = \frac{h_c^3}{3} + e h_c^2 + e^2 h_c \quad (10)$$

$$e = \frac{E_s h_s^2 - E_c h_c^2}{2 (E_s h_s + E_c h_c)} \quad (11)$$

In the above equations, the indexes c and t refer to the coating and the whole beam respectively.

$F_t$ : first flexural resonance frequency of the composite beam (substrate + film),

$\rho_{eff}$ : weighted area density (in  $kg/m^2$ ),

$e$ : the shift of the neutral axis after deposition.

In the case of a composite beam with a rectangular cross-section subjected to torsional vibrations, the shear modulus can be obtained from the following equation [17]:

$$R_T = \left[ \frac{\rho_s b (h_s^2 + b^2)}{3 G_s h_s^2 \left( b - \frac{h_s}{\sqrt{3}} \tanh \left[ \frac{\sqrt{3} b}{h_s} \right] \right)} \right]^{0.5} \left[ \frac{[A(3bCH_3(h_s E_s + h_c E_c) - H_4 \sqrt{3A})]}{[(bCH_3(h_s E_s + h_c E_c)(H_1 \rho_s h_s + H_2 \rho_c h_c))]} \right]^{0.5} \quad (12)$$

where:

$$R_T = \frac{T_t}{T_s} \quad (13)$$

$$A = E_s^2 h_s^5 G_s + E_c^2 h_c^5 G_c + E_s h_s^4 h_c (2E_c G_s + 3E_s G_c) + E_c h_s h_c^4 (2E_s G_c + 3E_c G_s) + 2h_s^3 h_c^2 (3E_s^2 G_c + 2E_c^2 G_s) + 2h_s^2 h_c^3 (2E_s^2 G_c + 3E_c^2 G_s) \quad (14)$$

$$B = 2\sqrt{3} b C (E_s h_s + E_c h_c) \quad (15)$$

$$C = \sqrt{G_s h_s + G_c h_c} \quad (16)$$

$$H_1 = 3h_s^3 E_s^2 (h_s + 2h_c) + E_c h_c (b^2 + h_c^2) (2h_s E_s + E_c h_c) + E_s^2 h_s^2 (b^2 + 4h_c^2) \quad (17)$$

$$H_2 = 3h_c^3 E_c^2 (h_c + 2h_s) + E_s h_s (b^2 + h_s^2) (2h_c E_c + E_s h_s) + E_c^2 h_c^2 (b^2 + 4h_s^2) \quad (18)$$

$$H_3 = \frac{B}{e^{\sqrt{A}} + 1} \quad (19)$$

$$H_4 = \frac{B}{e^{\sqrt{A}} - 1} \quad (20)$$

Using Eq. (5) to Eq. (20), the Young's and shear moduli of an isotropic thin film can be determined. In the following section (§2.3), the extension of this method to an elastic behavior of anisotropic thin films is presented.

### 2.3. Development of a model for an anisotropic coating

A simplified 1D model based on the laminated theory is developed in this section. It fulfills Kirchhoff hypotheses [22] and it is applicable for thin films with plane anisotropy. Using the plane-stress assumption, three of the six components of stress are generally much smaller than the other three. For a coated substrate, the stresses in the plane of the beam are much larger than the stresses perpendicular to that plane [22]. These negligible components can then be set to zero, which simplifies the solution.

From the relation between stresses and strains for the state of plane-stress and taking into account the shift of the neutral axis after deposition, the third-order bending stiffness matrix  $D_{ij}$  can be expressed as follows [18]:

$$D_{ij} = \int_{-h_s+e}^e \bar{Q}_{ij}^{(s)} z^2 dz + \int_e^{e+h_c} \bar{Q}_{ij}^{(c)} z^2 dz \quad (i, j = 1, 2 \text{ or } 6) \quad (21)$$

where:

$\bar{Q}_{ij}$  are the transformed reduced stiffness elements that are a function of the reduced stiffness elements  $Q_{ij}$ . The  $Q_{ij}$  elements are a function of the elasticity constants of the corresponding

layer. The shift of the neutral axis, in the case of the two beams, dependent on only one direction [23]. It is calculated in unidirectional by taking only the X component of the Young's modulus for each pair of beams, as follows:

$$\begin{pmatrix} e_{\Delta} \\ e_{\Pi} \end{pmatrix} = \frac{1}{2} \begin{pmatrix} \frac{E_s h_s^2 - E_{\Delta} h_c^2}{(E_s h_s + E_{\Delta} h_c)} \\ \frac{E_s h_s^2 - E_{\Pi} h_c^2}{(E_s h_s + E_{\Pi} h_c)} \end{pmatrix} \quad (22)$$

where  $\Delta$  and  $\Pi$  represent two perpendicular directions in the film surface plane.

Working with the X and Y as principal axes for both substrate and film, the stiffness elements become:

For isotropic substrate [22]:

$$\bar{Q}_{11}^{(s)} = Q_{11}^{(s)} = \bar{Q}_{22}^{(s)} = Q_{22}^{(s)} = \frac{E_s}{1 - \nu_s^2} \quad (23)$$

$$\bar{Q}_{12}^{(s)} = Q_{12}^{(s)} = \nu_s Q_{11}^{(s)} = \frac{\nu_s E_s}{1 - \nu_s^2} \quad (24)$$

$$\bar{Q}_{66}^{(s)} = Q_{66}^{(s)} = G_s = \frac{E_s}{2(1 + \nu_s)} \quad (25)$$

For anisotropic film [22]:

$$\begin{pmatrix} \bar{Q}_{11}^{(\Delta)} \\ \bar{Q}_{11}^{(\Pi)} \end{pmatrix} = \begin{pmatrix} Q_{11}^{(\Delta)} \\ Q_{11}^{(\Pi)} \end{pmatrix} = \frac{1}{1 - \nu_{\Pi\Delta} \nu_{\Delta\Pi}} \begin{pmatrix} E_{\Delta} \\ E_{\Pi} \end{pmatrix} \quad (26)$$

$$\begin{pmatrix} \bar{Q}_{22}^{(\Delta)} \\ \bar{Q}_{22}^{(\Pi)} \end{pmatrix} = \begin{pmatrix} Q_{22}^{(\Delta)} \\ Q_{22}^{(\Pi)} \end{pmatrix} = \frac{1}{1 - \nu_{\Pi\Delta} \nu_{\Delta\Pi}} \begin{pmatrix} E_{\Pi} \\ E_{\Delta} \end{pmatrix} \quad (27)$$

$$\begin{pmatrix} \bar{Q}_{12}^{(\Delta)} \\ \bar{Q}_{12}^{(\Pi)} \end{pmatrix} = \begin{pmatrix} Q_{12}^{(\Delta)} \\ Q_{12}^{(\Pi)} \end{pmatrix} = \frac{\nu_{\Pi\Delta}}{1 - \nu_{\Pi\Delta} \nu_{\Delta\Pi}} \begin{pmatrix} E_{\Delta} \\ E_{\Pi} \end{pmatrix} = \frac{\nu_{\Delta\Pi}}{1 - \nu_{\Pi\Delta} \nu_{\Delta\Pi}} \begin{pmatrix} E_{\Pi} \\ E_{\Delta} \end{pmatrix} \quad (28)$$

$$\bar{Q}_{66}^{(\Delta)} = \bar{Q}_{66}^{(\Pi)} = Q_{66}^{(\Delta)} = Q_{66}^{(\Pi)} = G_{\Delta\Pi} \quad (29)$$

where:

$E_{\Delta}$ : Young's modulus of the film along  $\Delta$  direction,

$E_{\Pi}$ : Young's modulus of the film along  $\Pi$  direction,

$\nu_{\Delta\Pi}$ : highest Poisson's ratio of the film,

$\nu_{\Pi\Delta}$ : lowest Poisson's ratio of the film,

$G_{\Delta\Pi}$ : in-plane shear modulus of the film.

Using the same development as the one found in the literature for the isotropic film [18], the frequency ratio becomes:

$$\begin{pmatrix} R_{F\Delta} \\ R_{F\Pi} \end{pmatrix} = \frac{2}{h_s} \sqrt{\frac{3\rho_s}{E_s \rho_{eff}}} \begin{pmatrix} \frac{1}{\sqrt{d_{\Delta\Delta}}} \\ \frac{1}{\sqrt{d_{\Pi\Pi}}} \end{pmatrix} \quad (30)$$

where  $d_{\Delta\Delta}$  and  $d_{\Pi\Pi}$  represent the (1,1) element of bending matrix  $[D]^{-1}$  that can be expressed as:

$$\begin{pmatrix} d_{\Delta\Delta} \\ d_{\Pi\Pi} \end{pmatrix} = \begin{pmatrix} \frac{\frac{R_{\Delta} E_s}{1-v_s^2} + \frac{H_{\Delta} E_{\Pi}}{1-\nu_{\Pi\Delta}\nu_{\Delta\Pi}}}{\left[ \frac{R_{\Delta} E_s}{1-v_s^2} + \frac{H_{\Delta} E_{\Delta}}{1-\nu_{\Pi\Delta}\nu_{\Delta\Pi}} \right] \cdot \left[ \frac{R_{\Delta} E_s}{1-v_s^2} + \frac{H_{\Delta} E_{\Pi}}{1-\nu_{\Pi\Delta}\nu_{\Delta\Pi}} \right] - \left[ \frac{\nu_s R_{\Delta} E_s}{1-v_s^2} + \frac{\nu_{\Pi\Delta} H_{\Delta} E_{\Delta}}{1-\nu_{\Pi\Delta}\nu_{\Delta\Pi}} \right]^2} \\ \frac{\frac{R_{\Pi} E_s}{1-v_s^2} + \frac{H_{\Pi} E_{\Delta}}{1-\nu_{\Pi\Delta}\nu_{\Delta\Pi}}}{\left[ \frac{R_{\Pi} E_s}{1-v_s^2} + \frac{H_{\Pi} E_{\Pi}}{1-\nu_{\Pi\Delta}\nu_{\Delta\Pi}} \right] \cdot \left[ \frac{R_{\Pi} E_s}{1-v_s^2} + \frac{H_{\Pi} E_{\Delta}}{1-\nu_{\Pi\Delta}\nu_{\Delta\Pi}} \right] - \left[ \frac{\nu_s R_{\Pi} E_s}{1-v_s^2} + \frac{\nu_{\Delta\Pi} H_{\Pi} E_{\Pi}}{1-\nu_{\Pi\Delta}\nu_{\Delta\Pi}} \right]^2} \end{pmatrix} \quad (31)$$

with:

$$\begin{pmatrix} R_{\Delta} \\ R_{\Pi} \end{pmatrix} = \frac{1}{3} \begin{pmatrix} e_{\Delta}^3 - (-e_{\Delta} + h_s)^3 \\ e_{\Pi}^3 - (-e_{\Pi} + h_s)^3 \end{pmatrix} \quad (32)$$

$$\begin{pmatrix} H_{\Delta} \\ H_{\Pi} \end{pmatrix} = \frac{1}{3} \begin{pmatrix} -e_{\Delta}^3 + (e_{\Delta} + h_c)^3 \\ -e_{\Pi}^3 + (e_{\Pi} + h_c)^3 \end{pmatrix} \quad (33)$$

#### 2.4. Finite element analysis

A 3D finite element model (FEM) was developed using the commercial finite element code ABAQUS [24] in order to check the reliability of the developed formulation. A comparison between the developed model and the FEM was performed. The geometrical model is composed of two parts: the substrate and the film. The composite structure was constructed by bonding the film on the substrate already created, through the ‘‘tie function’’. This function can be replaced by the ‘‘partition function’’ that gives similar results for the first four extracted frequencies.

The substrate has a length  $L$  of 70 mm, width  $b$  of 20 mm and thickness  $h_s$  of 1 mm with a rectangular cross-section. The film has the same length and width as the substrate with a thickness  $h_c$  that was varied from 0 to 0.5 mm. For linear elastic calculations, the 3D stress C3D20 quadratic element was used to mesh the composite beam. The mesh density was found equal to  $0.35 \times 0.27 \times 0.5 \text{ mm}^3$  for the substrate and the film. By using this mesh density, the values of the first four resonant frequencies converge, leading to invariant frequency values at the smallest mesh densities. A free-free boundary condition was applied to the composite.

The ABAQUS/Implicit Lanczos eigensolver is used to extract the resonant frequencies of the composite beam. Fig. 1 presents the first harmonic mode of a free-free coated beam in flexural and torsional vibrations. These configurations were chosen as a reference to validate

the developed analytical model. A parametric comparison of the analytical model with the FEM was done with a combination of different substrate and film Young's moduli.

Fig. 2 presents the evolution of the frequency ratio  $R_F$  as a function of the thickness ratio  $R_h$  (Eq. (34)) of the developed and the numerical models for four different anisotropic ratios  $AR_E$  (Eq. (35)). The  $AR_E$  are chosen to give examples of high and low anisotropy that can correspond to realistic situations.

$$R_h = \frac{h_c}{h_s} \quad (34)$$

$$AR_E = \frac{E_\Pi}{E_\Delta} = \frac{\nu_{\Pi\Delta}}{\nu_{\Delta\Pi}} \quad (35)$$

$$AR_G = \frac{G_{\Delta Z}}{G_{\Pi Z}} \quad (36)$$

The values of the elasticity constants **along the normal to the film surface (Z direction)** were assumed equal **to those in the film surface plane ( $\Delta$  or  $\Pi$  direction)**, since there is no influence of the perpendicular direction on the frequency found in the X-Y plane, **in the case of thin films**. The highest Poisson's ratio of the film  $\nu_{\Delta\Pi}$  was assumed equal to that for an isotropic material since the Poisson ratio has a negligible effect on the frequency determined using FEM for isotropic material [18].

From Fig. 2, a good agreement between the developed and the finite element calculations for low thickness ratio  $R_h$  can be observed. The difference between the two models increases with  $R_h$  and can be observed in Fig. 2(d) where the  $AR_E$  is the highest. This could be caused by the plane-stress state assumption on which is based the 1D analytical model while using the 3D FEM that does not make any assumptions. With the increase of  $AR_E$ , the coupling effect between the directions increases. The developed model neglects the coupling with the Z direction that becomes significant, owing to the increase in thickness. The difference between the analytical model and the FEM remains approximately constant by increasing the anisotropic ratio. In the rest of this work, glass substrates are used and the elasticity constants of Ti thin films with  $R_h < 0.05$  are determined using the developed model (Eq. (30)).

### 3. Experimental details

#### 3.1. Impulse Excitation Technique

The IET is used to measure the resonance frequencies of a sample impacted by a striker. Flexural, torsional and longitudinal vibrational modes can be obtained by vibrating a sample. In order to adopt a free-free boundary condition, the sample is placed on a support with negligible interaction i.e. nylon wires placed along the nodal lines of the fundamental flexural and torsional modes. The support wires are located at the nodal points of the sample, where the displacement is equal to zero. These conditions are the simplest to adopt because they represent the configuration with the least interaction between the support system and the specimen compared with the other configurations. An RFDA professional signal analysis system (Resonance Frequency and Damping Analysis) from IMCE Company (Genk, Belgium) was used to measure the resonant frequencies. It is equipped with an RFDA transducer, an acoustic microphone with a frequency range up to 100 kHz, a universal wire support, an automatic excitation unit and a computer system equipped with RFDA software. The mechanical vibrations produced by the sample are detected by an acoustic microphone. Then, the RFDA transducer transforms these vibrations into an electrical signal recorded as a function of time. The natural resonance frequencies of the sample are extracted by applying the Fast Fourier Transform (FFT) to the signal.

In the case of thin films, the vibration measurements were conducted sequentially with two-steps frequency measurements, i.e. firstly, the resonant frequencies of the substrates were determined, then the titanium film was deposited on each substrate and the resonant frequencies of the whole beam (substrate + film) were measured again. Using a mechanical model that contains the ratio between the two measured frequencies, the density and the dimensions of the substrate and the film, the elasticity constants **of the film** can be calculated by an inverse method. This methodology has been widely used in the literature [13-16].

The laminated theory considers that each layer acts like a lamina. In our case, it can be applicable for thin films with plane anisotropy under a plane-stress state. This presumption leads to identify the elasticity constants along two perpendicular directions  $\Delta$  and  $\Pi$ , defined in **Fig. 3**, on the film surface.

In the case of anisotropic films, the determination of the elasticity constants along two perpendicular directions seems to be easier by using a plate since it can be excited along its length and width axes. This method was used with the IET to determine the anisotropic moduli of a bulk plate [25,26]. Contrariwise, the analytical formulations **are rather complex** in

the case of a bulk plate, since they are 2D expressions and require the use of discretization methods and structural optimization with genetic algorithms [25].

In this work, the methodology used consists of depositing different pairs of coatings at an oblique incidence; the X-axis defined as the longest dimension of the specimen, (resp. Y-axis, defined as the transverse dimension) of the first sample in Fig. 4(a) coincides with the  $\Delta$  direction (resp.  $\Pi$  direction) presented in Fig. 3. The reciprocal perspective is often applied for the second sample (Fig. 4(b)), where the X-axis (resp. Y-axis) is parallel to the  $\Pi$  direction (resp.  $\Delta$  direction), to obtain tilted columns along two different perspectives at a constant glancing angle  $\alpha$ . The deposition process as well as sample positions are presented in §3.2.

In this way, each pair of beams is vibrated along the beam length leading to different frequency responses. After that, the developed model is used for each pair of beams to determine the elastic properties in each direction. This methodology allows us to simultaneously determine the unknown elasticity constants of the film using an analytical model.

### 3.2. Deposition procedure

Titanium thin films were deposited on glass substrates and silicon wafers with DC magnetron sputtering technique using a DEPHIS4 Physical vapor deposition (PVD) machine. A high purity (99.99 %) Ti circular target of 200 mm of diameter was used. The deposition chamber corresponds to a cylinder of 98 liters pumped down with a turbo-molecular pump to less than  $10^{-4}$  Pa before filling it with argon (Ar). The series was processed at a total working pressure of 0.35 Pa (Ar flow rate: 30 sccm) with a deposition time of 240 min. The intensity applied to the Ti target was 1.5 A using a DC-pulsed power supply. The target-to-substrate average distance was 220 mm.

Before the deposition process, the substrates were ultrasonically cleaned in acetone and ethanol for 10 min. The Ti target was sputter-cleaned for 15 min in pure Ar discharge, while a shutter shielded the substrates. Individual aluminum holders with different inclinations with respect to the main plate holder were fabricated to vary the glancing angle  $\alpha$  of the substrates. The holders used carried three orientations  $\alpha = 0^\circ$ ,  $45^\circ$  and  $80^\circ$  for deposition with respect to the target normal as illustrated in Fig. 5. These three orientations were chosen in order to analyze different critical configurations. The substrates were located on the holder in specific positions in order to minimize self-shadowing [4,27].

The investigated samples consisted of six glass substrates for the IET and NI tests and six silicon wafers for the scanning electron microscopy (SEM) images. All the samples were

prepared in a single deposition event. The positioning of the samples in the chamber during the deposition is schematically depicted in Fig. 6. The samples were paired. The vertical beams (shown in blue in Fig. 6) correspond to the samples deposited along the longitudinal direction (Fig 4(a)) while the horizontal beams (shown in red in Fig 6) correspond to the samples deposited along the transverse direction (Fig. 4(b)). The sample naming  $A_{0,X}$ ,  $A_{45,X}$  and  $A_{80,X}$  stands for the vertical beams (Fig. 4(a)) deposited at  $0^\circ$ ,  $45^\circ$  and  $80^\circ$  of inclination, respectively. On the other hand, the horizontal beams (Fig. 4(b)) deposited at  $0^\circ$ ,  $45^\circ$  and  $80^\circ$  of inclination, are represented by  $A_{0,Y}$ ,  $A_{45,Y}$  and  $A_{80,Y}$ , respectively.

### 3.3. *Dimensions and density*

The dimensions of each substrate were measured ten times in ten different positions using a digital micrometer screw gauge. The average dimensions and their uncertainties are presented in Table 1. The film thickness was measured from the cross-sectional view using the SEM images. Note that the film thickness is defined as the vertical thickness of the film i.e. measured along the substrate normal, which may be different from the length of a column element depending on the column shape and orientation. The average and uncertainty of ten different thickness measures were taken. The standard uncertainties on the measured dimensions were evaluated using a type A method by computing the standard deviation [28].

The mass of the substrate was measured using a Sartorius precision balance and then the density was calculated from the mass over volume. The uncertainties on the substrate mass were evaluated following a type B procedure [28]. According to technical specifications of the precision balance used, the uncertainty is equal to 0.1 mg. After deposition, the mass of the composite beam was measured. The measured mass and density of the substrates and films are also presented in Table 1 with the measurement uncertainty.

The uncertainty analysis was performed using the guidelines of the expressions of uncertainty in measurement [28] and precisely estimating the main sources of uncertainty: frequency, thickness and density. This metrological procedure was studied in detail in previous publications, where the contribution of each uncertainty source on the Young's modulus was given [14,18].

### 3.4. *Microstructure*

The grain morphology of the deposited titanium films was analyzed using a Hitachi S3500 N SEM-FEG. In order to identify the crystalline structure of the Ti films, a Bruker D8 Advance diffractometer equipped with a  $\text{CuK}\alpha$  tube radiation ( $\lambda = 0.15418$  nm) operated at

40 kV and 40 mA was used to acquire X-ray diffraction patterns (XRD). A point focus mode with a 1 mm collimator was used for the incident beam. The diffractometric angle  $2\theta$  was varied between  $30^\circ$  and  $150^\circ$ . In order to acquire the sum of the X-ray diffraction patterns as well as pole figures, the azimuth angle  $\phi$  was varied between  $0^\circ$  and  $360^\circ$  with  $10^\circ$  of increment and the tilt angle  $\psi$  was varied between  $0^\circ$  and  $70^\circ$  with  $10^\circ$  of increment.

### 3.5. Nanoindentation

The hardness and reduced Young's modulus of the Ti films were measured using a TriboIndenter TI 980-Hysitron with continuous stiffness measurement (CSM) option. A Berkovich diamond tip ( $E_{ind} = 1140$  GPa,  $\nu_{ind} = 0.07$ ) was used to perform indentations. For calibration before performing tests, a polycarbonate glass specimen was used. The hardness and reduced Young's modulus of the indented material can be determined using the Oliver and Pharr method [29]. The hardness can be determined from its usual definition:

$$H = \frac{P_{max}}{A_c} \quad (37)$$

where  $H$  is the hardness,  $P_{max}$  is the maximum load applied to the indented material and  $A_c$  is the projected contact area. The reduced Young's modulus can be deduced from the following equation [29]:

$$\frac{1}{E^r} = \frac{1}{E_c^r} - \frac{1 - \nu_{ind}^2}{E_{ind}} \quad (38)$$

where  $E^r$  is the reduced Young's modulus,  $E_{ind}$  and  $\nu_{ind}$  are respectively the Young's modulus and the Poisson's ratio of the indenter and  $E_c^r$  is the contact-reduced modulus of the sample and the indenter, which is expressed as below [29]:

$$E_c^r = \frac{S}{2k} \sqrt{\frac{\pi}{A_c}} \quad (39)$$

where  $S$  is the contact stiffness and  $k$  is a correction factor depending on the indenter geometry.

The film hardness and reduced modulus were determined from the average of ten indents and the uncertainty of measurements  $u(x)$  was determined from the standard deviation. In order to minimize the effect of the substrate on the film hardness and reduced modulus measurements, the indenter penetration depth was kept lower than 10 % of the film thickness [30] controlled by the indenter penetration load.

## 4. Morphology

Fig. 7(a) shows the fracture cross-sectional SEM images of the Ti films sputter-deposited at 0.35 Pa. The growth morphology of all films exhibits a well-defined columnar growth, as commonly observed for Ti films [4,5,31]. For zero incidence ( $\alpha = 0$ ), the resulting structure is only slightly porous since no significant shadowing is achieved and the micro-columns are not separated. As the glancing angle increases, the shadowing effect increases progressively and the structure becomes more porous. With increasing the glancing angle  $\alpha$ , the inclination of the columns with respect to the substrate normal increases. The angle between the columns and the substrate normal is defined by  $\beta$  (Fig. 7(a)). It is noticeable that the columns boundaries become more distinctive with increasing the glancing angle  $\alpha$ . In the beginning, a self-shadowing of the initial particles was formed on the substrate surface. These nuclei keep growing to form successive columns separated by voids due to the inclination that favors the shadows (Fig. 8).

The surface topography of the films is presented in Fig. 7(b). The film surface is considerably influenced by the glancing angle  $\alpha$ , as mentioned in the literature [4,5,32,33]. At normal incidence ( $\alpha = 0^\circ$ ), the tops of the columns appear at the film surface with circular facets suggesting a low inter-columnar porosity fraction. As the glancing angle increases, the shadowing effect predominates and the gap between columns significantly increases, providing a higher fraction of inter-columnar porosity. It is necessary to notice that an in-plane anisotropic shadowing is formed, which is the aim of the GLAD technique. All the columns face the incoming flux, which is indicated by an arrow. This can be visible with the in-plane arrangement of the columns at  $\alpha = 80^\circ$ , for which, the columns are well distributed in the transverse direction of the incident flux.

The column tilt angle  $\beta$  is ordinarily lower than the glancing angle  $\alpha$  due to the shadowing effect and it is measured from the cross-sectional SEM images. In order to improve the accuracy of the measured values of  $\beta$ , the average of ten column tilt angle measurements was taken. The measurement uncertainty of  $\beta$  was estimated from the standard deviation over the ten columns. The experimental  $\beta$  values can be compared with several models proposed in the literature providing different predictive relationships between  $\alpha$  and  $\beta$ . One of them is called “tangent rule”, which is a semi-empirical formula and it is applicable only for  $\alpha < 50^\circ$  since it is not derived from a physical model [34]:

$$\tan \beta_{tan} = \frac{1}{2} \tan \alpha \quad (40)$$

Another relationship was reported to provide a physically based description of the growth mechanics with a geometrical analysis of the inter-columnar geometry. It is called “cosine rule” and was derived by Tait et al. [35] as follows:

$$\beta_{cos} = \alpha - \arcsin\left(\frac{1 - \cos \alpha}{2}\right) \quad (41)$$

This is a purely geometrical equation. It takes into account the ballistic shadowing growth mechanism without considering the growth kinetics [27].

## 5. Characterizations

### 5.1. Crystalline structure and texture evolution

The XRD patterns of the deposited titanium films are presented in Fig. 9, for the three values of the glancing angle  $\alpha$ . The identification of the titanium film phases was performed on the sum of the diffraction patterns collected in the range of azimuth and tilt angles mentioned above. It can be clearly seen that all structures exhibit a single hexagonal closed packed (hcp)  $Ti_{\alpha}$  stable phase, compared to the reference powder diffraction data (ICDD card n°44-1294, P63/mmc). This structure was observed on pure titanium films deposited by different techniques [36,37]. It can be noted that the relative intensity of the  $(0002)$  diffracted plane is higher than that of the reference data. As we will see in the texture analysis below, it is due to a  $[0002]$  preferred orientation developed in the Ti films.

Fig. 10 shows the experimental pole figures measured for two diffraction peaks that correspond to  $\{0002\}$  and  $\{10\bar{1}1\}$  planes of the  $Ti_{\alpha}$  phase. In order to perform the texture measurements, the samples were placed on the XRD stage so that the incident flux direction lies with the goniometer azimuthal angle  $\phi$  of  $270^{\circ}$ . This direction was chosen as a reference for all samples and the arrows shown in Fig. 10 correspond to the incident flux direction. At normal incidence ( $\alpha = 0^{\circ}$ ), the pole figure of the  $\{0002\}$  plane exhibits a maximum diffracted intensity approximately at the center with a small inclination of  $7^{\circ} \pm 3^{\circ}$ . This small deviation of the texture is usual in such sputtering processes and can be due to small angular spread between the substrate normal and the vapor flux direction [38].

The  $\{10\bar{1}1\}$  pole figure shows a ring around the  $7^{\circ}$  shifted center with an inclination angle  $\psi$  of  $61.3^{\circ} \pm 0.5^{\circ}$ , which is coherent with the angle between  $(0002)$  and  $(10\bar{1}1)$  planes in a hexagonal symmetry. It shows an out-of-plane fiber texture of the film along the  $[0002]$  direction that explains the high intensity of the  $(0002)$  diffracted plane shown on the XRD

pattern. These indications show that the crystalline growth is faster along the c-axis of the crystal than along other directions.

For a glancing angle of  $45^\circ$  and  $80^\circ$ , the shadowing effect becomes significant and the columns are tilted approximately by  $5^\circ \pm 3^\circ$  and  $21^\circ \pm 3^\circ$  respectively as shown in the cross-sectional SEM images (Fig. 7). The experimental pole figure of the  $\{0002\}$  plane in Fig. 10(a) shows that the fiber texture axis is tilted by  $30^\circ \pm 3^\circ$  for  $\alpha = 45^\circ$  and  $46^\circ \pm 3^\circ$  for  $\alpha = 80^\circ$  with respect to the surface normal towards the direction of the incoming vapor flux. The fiber tilt angle is defined by  $\eta$ . During the initial nucleation, each nucleus grows on the substrate, forming crystals with a random orientation before the collision between neighboring crystals. When the diffusion from one crystal to another occurs, the crystal providing the most tilted facets will predominate. Then, this prevalent crystal will cover the neighbors allowing an out-of-plane texture of the film with its own preferred orientation. This phenomenon is influenced not only by the geometry of the vapor incident flux but also by the kinetics of crystallite growth [33]. The reader can refer to Mahieu et al. [33] for more explanation about the formation of the out-of-plane texture.

This tilting of the fiber axis with respect to the film normal was also shown in Ti [36,39], Mo [40], Mg [41], HfN [42], TiN [32] and AlN [43] thin films. Table 1 summarizes the glancing angle  $\alpha$ , columns tilt angle  $\beta$  and the fiber tilt angle  $\eta$ . Compared to the theoretical values of  $\beta_{cos}$  and  $\beta_{tan}$ , the experimental column tilt angle  $\beta$  presents large deviations (Table 1). This can be due to the ballistic parameters that affect the column tilt angle like the working pressure [5,32], the crystalline structure [31], the temperature [36] or the geometry of the target [31]. Contrariwise, it can be noticed that the angle calculated using the well-known “cosine rule” is in coherence with the experimental fiber tilt angle  $\eta$  at least in the present case. This is being explained by the physical approach on which the “cosine rule” is based [35].

Furthermore, the fiber tilt angle  $\eta$  is not equal to the column tilt angle  $\beta$  as can be seen in Table 1, i.e. the crystalline growth direction does not correspond to the column growth direction. The observations reported in the literature for the hcp crystallites show that the texture formation strongly depends on the material component [44]. For instance, the two axes (column axis and c-axis) are not equal for Ti-hcp films [36,39] and in contrast, can coincide for Co-hcp in Co-Cr films [44] and Mg-hcp films [41]. Fig. 11 illustrates the microstructural configuration found in our case.

The XRD measurements correspond to the Ti films deposited on the vertical beams ( $A_{0,X}$ ,  $A_{45,X}$  and  $A_{80,X}$ ) with the X-axis coincides with the  $\Delta$  direction. Very similar XRD patterns and pole figures measurement were observed for the Ti films deposited on the horizontal beams (not shown here). These pole figures lead to the presence of an in-plane anisotropic structure of the film. This requires the use of the developed model (Eq. (30)) in order to determine the elasticity constants of these anisotropic coatings.

## 5.2. Elasticity constants of the deposited titanium films

The flexural and torsional resonance frequencies of the samples, measured by the IET before and after deposition, are presented in Table 2. The different sources of uncertainty on the measured frequencies were determined from a series of experimental measurements on the IET in previous work [14]. The uncertainty of the fundamental resonance frequency was found equal to 0.117 Hz. The film thickness range that is suitable to have a reliable method depends on the film material and the degree of anisotropy. For this, the thickness ratio  $R_h$  should be selected in order to have a frequency shift higher than the uncertainty on the measured frequency. Using IET with the fundamental harmonic mode, the frequency shift should be higher than 0.117 Hz to reliably apply this methodology. From Table 2, we can notice that the frequency shift after deposition is largely higher than the frequency uncertainty.

The elasticity constants of the glass substrates (assumed isotropic) were determined using Eq. (1) and Eq. (2). They are presented with the measurement uncertainties in Table 2. The analytical expression of the developed model (Eq. (30)) represents an implicit function. The uncertainties on the elasticity constants were calculated using Monte Carlo's method by generating a random dispersion over the experimental values.

The Young's moduli  $E_\Delta$  and  $E_\Pi$  of the titanium film were determined using the developed formulation (Eq. (30)) assuming  $\nu_{\Delta\Pi} = \nu_{isotropic} = 0.32$  [45] and  $\nu_{\Pi\Delta} = \nu_{\Delta\Pi} \frac{E_\Pi}{E_\Delta}$  [22]. The shear moduli  $G_{\Pi Z}$  and  $G_{\Delta Z}$  of the titanium films were determined using Eq. (12) with  $E_\Delta$  and  $E_\Pi$  respectively. The shear moduli were determined by taking the corresponding Young's modulus and using the isotropic model. Using the  $\Delta$  and  $\Pi$  components, the torsional vibrations are produced in  $\Pi$ -Z and  $\Delta$ -Z planes respectively. Moreover, Table 2 presents the elasticity constants and the anisotropic ratios  $AR_E$  (Eq. (35)) and  $AR_G$  (Eq. (36)) with their corresponding uncertainty as a function of the glancing angle  $\alpha$ . The Young's moduli are also

determined using Eq. (5) in order to compare the directional moduli ( $E_{\Delta}$  and  $E_{\Pi}$ ) determined simultaneously to the ones determined independently by vibrating along X-axis ( $E_X$ ).

The elasticity constants of glass and titanium found in the literature are presented in Table 3. We can notice that the macroscopic elasticity constants of the glass substrates are consistent with the literature values [17,18,20]. The values of the titanium film Young's modulus, presented in Table 2, varied from 15.63 to 99.56 GPa. The values published in the literature for Ti thin films are highly dispersed: the values found in the present work are consistent with some of them [18,45,46] and differ from some others [47,48]. From Table 2, we can notice that the values of the elasticity constants are lower than those reported for bulk titanium (Table 3). This is attributed to the microstructural features due to the GLAD process and its effect on the film elastic properties. However, we can notice that the anisotropic Young's moduli are in good agreement with those calculated independently from Eq. (5). This can be explained by the negligible effect of the elastic coupling between  $E_{\Delta}$  and  $E_{\Pi}$ , defined in  $d_{\Delta\Delta}$  and  $d_{\Pi\Pi}$  of Eq. (31). These results allow us to conclude that the IET leads to a correct value of Young's modulus toward a proper direction even if it is used with the isotropic model instead of the anisotropic one.

### 5.3. Hardness and reduced modulus of obliquely deposited titanium films

Fig. 12 presents the evolution of hardness  $H$  and reduced modulus  $E^r$  of the Ti films as a function of the glancing angle  $\alpha$ . The measurements were performed on horizontal and vertical samples. The hardness and reduced modulus remain relatively constant when increasing the glancing angle to  $45^\circ$ . When performing the NI test, the change in the mechanical properties of Ti films was noticed in the literature for  $\alpha \geq 60^\circ$  [31]. At  $80^\circ$  of glancing angle, we can notice the decrease in hardness and reduced modulus of the Ti film. As discussed in the previous section, this can be due to the increase in porosity with the glancing angle.

Furthermore, the dashed lines in Fig. 12 correspond to the values at zero incidences ( $H_0, E_0^r$ ) correlated through the cosine of the columns tilt angle. A good agreement is noticed between the correlation and the NI values of the Ti films for  $\alpha \leq 45^\circ$ . This result allows us to assume that the load applied by the indenter is transmitted through the column axis. At  $80^\circ$  of glancing angle, this correlation is no longer valid since the contribution from friction or bending of the columns becomes significant. It toggles the results and the prediction of the hardness and reduced modulus for  $\alpha > 45^\circ$ , since the contribution of the frictions and the

bending moments of the columns has assumed negligible [3,7]. Consequently, the variation of the elasticity constants of the Ti films is due to the microstructure. One of the microstructural parameters is the film porosity, which is affected by the deposition parameters and notably the glancing angle  $\alpha$ .

The nanoindentation measurements and the correlation were performed to understand the evolution of the hardness and reduced Young's modulus as a function of the microstructure. Their results were not used for comparison with those measured by IET.

#### 5.4. Effect of film porosity on the elasticity constants

In order to verify that the porosity affects the elasticity constants values, two relations (Eq. (42) and Eq. (43)) proposed by Nemat-Nasser et al. [49] are used. The porosity was assumed isotropic in the model i.e. the pores were considered as spherical inclusions. These relations are applicable to determine the elasticity constants of the Ti film as follows:

$$E^* \approx E_0(1 - 3p) \quad (42)$$

$$G^* \approx G_0 \left(1 - \frac{4p}{1 + \nu_0}\right) \quad (43)$$

where:

$E, G$ : Young's and shear moduli of the material with porosity,

$E_0, G_0, \nu_0$ : Young's, shear moduli and Poisson's ratio of the material that are free of pores

(here we used  $E_0 = 116$  GPa [45],  $\nu_0 = 0.32$  [45],  $G_0 = \frac{E_0}{2(1+\nu_0)}$ ),

$p$ : volume fraction of porosity.

The volume fraction of porosity within the Ti films is estimated as follows [38]:

$$p = 1 - \frac{\rho_c}{\rho_0} \quad (44)$$

where:

$\rho_c$ : film density,

$\rho_0$ : bulk density without pores.

In this study, the volume fraction of porosity is calculated using Eq. (44) by comparing the film density to the bulk one.

The porosity assessment was also carried out by image analysis using ImageJ software [50]. Image analysis of SEM top-view images is done by pixel-based measurement, once the microstructure is digitized. The porosity zone was estimated by masking the processed SEM microstructure as a binary image with different thresholding levels. This method was

accurately performed on five different SEM images of each glancing angle and the mean value with the uncertainty of the area fraction of porosity were quantified.

Table 2 presents the values of film porosity calculated using Eq. (44) and image analysis, the Young's and shear moduli calculated using respectively Eq. (42) and Eq. (43). From either Eq. (44) or image analysis, the results proved that the porosity within the Ti films increases by increasing the glancing angle. The difference between the values obtained using the two approaches is lower than the measurement uncertainties. The differences ( $E^{IET} - E^*$ ) and ( $G^{IET} - G^*$ ) between the elasticity constants measured by IET and those calculated with porosity are also presented in Table 2. These differences correspond to the contribution of the microstructure. We can notice that the influence of the microstructure on the measured Young's moduli becomes significant at 45° and 80° of incidence, where this influence is higher than the measurement uncertainty. Theoretically, this comparison can be used to represent the overall influence of the microstructural properties, as a whole, on the elasticity constants of such type of films. Nevertheless, their influence needs to be quantified and dissociated in order to determine the contribution of each microstructural parameter (morphology ( $\beta$ ), texture ( $\eta$ ), etc.) on the elasticity constants of thin films. This effect will be investigated in our future work.

## 6. Conclusions

This work presents an enhancement in the determination of the macroscopic elasticity constants of thin films with anisotropic behavior. Titanium thin films were sputter-deposited with inclined configuration. An enhanced formulation was developed allowing the determination of the elasticity constants of a coating by means of the Impulse Excitation Technique. The model was validated by comparing the results to those obtained from a numerical finite element model.

Ti thin films were sputter-deposited on inclined glass substrates and Si wafers with three different deposition glancing angles ( $\alpha = 0^\circ, 45^\circ$  and  $80^\circ$ ). Several substrate-holders were fabricated to obtain the same deposition conditions for all inclined samples. Analyses of morphology, crystalline structure and texture development of Ti thin films deposited at different glancing angles were performed.

A porous microstructure with columnar growth was formed. Upon increasing the glancing angle to 45° and 80°, the micro-columns formed were tilted respectively by 5° and 21° toward the vapor flux direction. X-ray diffraction characterization revealed the presence

of a single hcp  $Ti_{\alpha}$  phase. Moreover, the film exhibited an out-of-plane  $\{0002\}$  fiber texture oriented along the c-axis of the crystallites. The fiber texture was tilted with the c-axis to follow the vapor flux direction. For zero incidence ( $\alpha = 0$ ), the  $[0002]$  fiber axis was relatively tilted. The fiber tilt angle becomes  $30^{\circ}$  and  $46^{\circ}$  at glancing angles of  $45^{\circ}$  and  $80^{\circ}$  respectively. The shadowing effect led to the mechanism behind the micro-columns tilt angle. The crystallites were kinetically grown to form a preferred orientation related to their evolutionary growth habit.

The effect of film porosity on the elasticity constants of the Ti film was evaluated. It is noteworthy that the elasticity constants are mostly affected by the volume fraction of porosity. The elasticity constants of the Ti film determined using IET were in good agreement with the values determined by taking into account the film porosity. The anisotropic ratios,  $\frac{E_{\Pi}}{E_{\Delta}}$  and  $\frac{G_{\Delta Z}}{G_{\Pi Z}}$  increase from 0.96 and 0.98 to 4.18 and 1.59 respectively. Although, the hardness and the reduced modulus measured by nanoindentation decreased with increasing the glancing angle.

The mechanical properties of GLAD films are necessary in order to use them at the forefront of engineering and materials science. The future improvement of nanostructured thin films requires further study on the determination of their mechanical properties taking into account their functional structure, texture development and porosity.

## Declaration of competing interest

The authors declare that they have no known competing financial interests or personal relationships that could have appeared to influence the work reported in this paper.

## Acknowledgments

The authors would like to thank the co-founders of CERA project: The European Union (Fond Européen de Développement Régional), the GIP 52 (Groupement d'Intérêt Public Haute-Marne) and the Doctoral School in Sciences and Technology at the Lebanese University (Réseau UT/INSA-UL).

## Data availability

The raw/processed data required to reproduce these findings are available from the corresponding author upon reasonable request.

## References

- [1] A. Kundt, Ueber die electromagnetische drehung der polarisationsebene des lichten im eisen, *Annalen der Physik* 263 (1886) 191–202.
- [2] A. Lakhtakia, Sculptured thin films: accomplishments and emerging uses, *Mater. Sci. Eng. C* 19 (2002) 427-434.
- [3] J. Lintymer, N. Martin, J.-M. Chappé, P. Delobelle, and J. Takadoum, Nanoindentation of chromium zigzag thin films sputter deposited, *Surf. Coat. Technol.* 200 (2005) 269– 272.
- [4] A. Barranco, A. Borrás, A.R. Gonzalez-Elipe, and A. Palmero, Perspectives on oblique angle deposition of thin films: from fundamentals to devices, *Prog. Mater. Sci.* 76 (2016) 59–153.
- [5] J. Dervaux, P.A. Cormier, P. Moskovkin, O. Douheret, S. Konstantinidis, R. Lazzaroni, S. Lucas, and R. Snyders, Synthesis of nanostructured Ti thin films by combining glancing angle deposition and magnetron sputtering: a joint experimental and modeling study, *Thin Solid Films* 636 (2017) 644–657.
- [6] J.J. Roa, V. Rico, M. Oliva-Ramírez, A.R. González-Elipe, and E. Jiménez-Piqué, Nanoindentation and scratch resistance of multilayered TiO<sub>2</sub>-SiO<sub>2</sub> coatings with different nanocolumnar structures deposited by PV-OAD, *J. Phys. D: Appl. Phys.* 49 (2016) 135104 (7pp).
- [7] E. Jiménez-Piqué, L. González-García, V.J. Rico, and A.R. González-Elipe, Nanoindentation of nanocolumnar TiO<sub>2</sub> thin films with single and stacked zig-zag layers, *Thin Solid Films* 550 (2014) 444–449.
- [8] A.R. Shetty, A. Karimi, and M. Cantoni, Effect of deposition angle on the structure and properties of pulsed-DC magnetron sputtered TiAlN thin films, *Thin Solid Films* 519 (2011) 4262–4270.
- [9] R.R. Gräter, Z. Khan, R. Paxman, J.W. Ndieyira, B. Dueck, B.A. Bircher, J.L. Yang, U. Drechsler, M. Despont, R.A. McKendry, and B.W. Hoogenboom, Disentangling mechanical and mass effects on nanomechanical resonators, *Applied Physics Letters* 96 (2010) 023113.
- [10] S. Ma, H. Huang, M. Lu, and M. Veidt, A simple resonant method that can simultaneously measure elastic modulus and density of thin films, *Surface and Coatings Technology* 209 (2012) 208–211.
- [11] B. Ilic, S. Krylov, and H.G. Craighead, Young's modulus and density measurements of thin atomic layer deposited films using resonant nanomechanics, *Journal of Applied Physics* 108 (2010) 044317.

- [12] I. Stachiv, D. Vokoun, and Y-R. Jeng, Measurement of Young's modulus and volumetric mass density/thickness of ultrathin films utilizing resonant based mass sensors, *Applied Physics Letters* 104 (2014) 083102.
- [13] A. López-Puerto, F. Avilés, F. Gamboa, and A.I. Oliva, A vibrational approach to determine the elastic modulus of individual thin films in multilayers, *Thin Solid Films* 565 (2014) 228–236.
- [14] M.F. Slim, A. Alhussein, A. Billard, F. Sanchette, and M. François, On the determination of Young's modulus of thin films with impulse excitation technique, *J. Mater. Res.* 32 (2017) 497-511.
- [15] E. Zgheib, A. Alhussein, M.F. Slim, K. Khalil, and M. François, Towards a new methodology for measuring the macroscopic Young's modulus of multilayer thin films using impulse excitation technique, 24ème Congrès Français de Mécanique, Brest, 26 au 30 Août 2019.
- [16] M.F. Slim, A. Alhussein, E. Zgheib, and M. François, Caractérisation micro/macromécanique de l'élasticité des couches minces par modélisation multiéchelle, diffraction des rayons X et technique d'excitation impulsionnelle, 24ème Congrès Français de Mécanique, Brest, 26 au 30 Août 2019.
- [17] M.F. Slim, A. Alhussein, F. Sanchette, B. Guelorget, and M. François, An enhanced formulation to determine the Young's and shear moduli of thin films by means of impulse excitation technique, *Thin Solid Films* 631 (2017) 172–179.
- [18] E. Zgheib, A. Alhussein, M.F. Slim, K. Khalil, and M. François, Multilayered models for determining the Young's modulus of thin films by means of impulse excitation technique, *Mechanics of Materials* 137 (2019) 103143.
- [19] P. Gadaud, and S. Pautrot, Application of the dynamical flexural resonance technique to industrial materials characterization. *Mater. Sci. Eng., A* 370 (2004) 422–426.
- [20] P. Gadaud, X. Milhet, and S. Pautrot, Bulk and coated materials shear modulus determination by means of torsional resonant method, *Mater. Sci. Eng. A* 521–522 (2009) 303–306.
- [21] M.F. Slim, A. Alhussein, and M. François, Elasticity constants of a two-phase tungsten thin film. In: *ICEM Proceedings*, MDPI (2018).
- [22] M.W. Hyer, *Stress Analysis of Fiber-Reinforced Composite Materials*, first ed. DEStech publications Inc., Lancaster (2009).
- [23] J. Gere, *Mechanics of Materials* (Cengage Learning, Independence, 2003).
- [24] *Abaqus Analysis User's Manual* (6.12).

- [25] C. Maletta, and L. Pagnotta, On the determination of mechanical properties of composite laminates using genetic algorithms, *International Journal of Mechanics and Materials in Design* 1 (2004) 199–211.
- [26] E. Barkanov, M. Wesolowski, W. Hufenbach, and M. Dannemann, An effectiveness improvement of the inverse technique based on vibration tests, *Computers and Structures* 146 (2015) 152–162.
- [27] M.M. Hawkeye, M.T. Taschuk, and M.J. Brett, *Glancing angle deposition of thin films: Engineering the nanoscale*, John Wiley & Sons, 2014.
- [28] JCGM, 100:2008(E), *Evaluation of Measurement Data — Guide to the Expression of Uncertainty in Measurement*, 2008.
- [29] W.C. Oliver, and G.M. Pharr, Measurement of hardness and elastic modulus by instrumented indentation: advances in understanding and refinements to methodology, *J. Mater. Res.* 19 (1) (2004).
- [30] H. Buckle, *L'essai de microdureté et ses applications*, Publications Scientifiques et Techniques du Ministère de l'Air, ISSN 0370-1999, 1960.
- [31] A. Siad, A. Besnard, C. Nouveau, and P. Jacquet, Critical angles in DC magnetron glad thin films, *Vacuum* 131 (2016) 305–311.
- [32] B. Bouaouina, C. Mastail, A. Besnard, R. Mareus, F. Nita, A. Miche, and G. Abadias, Nanocolumnar TiN thin film growth by oblique angle sputter-deposition: experiments vs. simulations, *Mater. Des.* 160 (2018) 338–349.
- [33] S. Mahieu, P. Ghekiere, D. Depla, and R. De Gryse, Biaxial alignment in sputter deposited thin films, *Thin Solid Films* 515 (2006) 1229–1249.
- [34] J.M. Nieuwenhizen, and H.B. Haanstra, Microfractography of thin films, *Philips Tech. Rev.* 27 (1966) 87-90.
- [35] R.N. Tait, T. Smy, and M.J. Brett, Modelling and characterization of columnar growth in evaporated films, *Thin Solid Films* 226 (1993) 196–201.
- [36] S. Sadeghi-Khosravieh, and K. Robbie, Morphology and crystal texture in tilted columnar micro-structured titanium thin film coatings, *Thin Solid Films* 627 (2017) 69–76.
- [37] V. Chawla, R. Jayaganthan, A.K. Chawla, and R. Chandra, Morphological study of magnetron sputtered Ti thin films on silicon substrate. *Mater. Chem. Phys.* 111 (2008) 414–418.
- [38] M.F. Slim, A. Alhussein, E. Zgheib, and M. François, Determination of single-crystal elasticity constants of the beta phase in a multiphase tungsten thin film using impulse

excitation technique, X-ray diffraction and micro-mechanical modeling, *Acta Mater.* 175 (2019) 348–360.

[39] S. Liedtke, C. Grüner, J. W. Gerlach, A. Lotnyk, and B. Rauschenbach, Crystalline Ti-nanostructures prepared by oblique angle deposition at room temperature, *Journal of Vacuum Science and Technology B, Nanotechnology and Microelectronics: Materials, Processing, Measurement, and Phenomena* 36 (2018) 031804.

[40] S. Liedtke-Grüner, C. Grüner, A. Lotnyk, J.W. Gerlach, M. Mensing, P. Schumacher, and B. Rauschenbach, Crystallinity and texture of molybdenum thin films obliquely deposited at room temperature, *Thin Solid Films* 685 (2019) 8–16.

[41] F. Tang, G-C. Wang, and T-M. Lu, In situ reflection high energy electron diffraction surface pole figure study of biaxial texture evolution in anisotropic Mg nanoblades during shadowing growth, *J. Appl. Phys.* 102 (2007) 014306.

[42] G. Abadias, F. Anđay, R. Mareus, and C. Mastail, Texture and stress evolution in HfN films sputter-deposited at oblique angles, *Coatings* 9 (2019) 712.

[43] N.S. Dellas, and J.M.E. Harper, Effect of deposition angle on fiber axis tilt in sputtered aluminum nitride and pure metal films, *Thin Solid Films* 515 (2006) 1647–1650.

[44] A. Hagemeyer, H.J. Richter, H. Hibst, V. Maier, and L. Marosi, Crystallographic texture and morphology of obliquely deposited Co–Cr magnetic thin films on flexible polymeric substrates, *Thin Solid Films* 230 (1993) 199–202.

[45] M. Leonhardt, D. Schneider, J. Kaspar, and S. Schenk, Characterizing the porosity in thin titanium films by laser-acoustics, *Surf. Coat. Technol.* 185 (2004) 292– 302.

[46] T. Tsuchiya, M. Hirata, and N. Chiba, Young's modulus, fracture strain, and tensile strength of sputtered titanium thin films, *Thin Solid Films* 484 (2005) 245–250.

[47] M. Chinmulgund, R.B. Inturi, and J.A. Barnard, Effect of Ar gas pressure on growth, structure, and mechanical properties of sputtered Ti, Al, TiAl, and Ti<sub>3</sub>Al films, *Thin Solid Films* 270 (1995) 260–263.

[48] H. Savaloni, A. Taherizadeh, and A. Zندهnam, Residual stress and structural characteristics in Ti and Cu sputtered films on glass substrates at different substrate temperatures and film thickness. *Phys. B: Condens. Mat.* 349 (2004) 44–55.

[49] S. Nemat-Nasser, and M. Hori, *Micromechanics: Overall properties of heterogeneous materials*, Elsevier Science Publishers B. V, North-Holland-Amsterdam (1993).

[50] W.S. Rasband, ImageJ, U. S. National Institutes of Health, Bethesda, Maryland, USA, 2017 (<http://imagej.nih.gov/ij/>, n.d. <http://imagej.nih.gov/ij/>).

## List of Figures

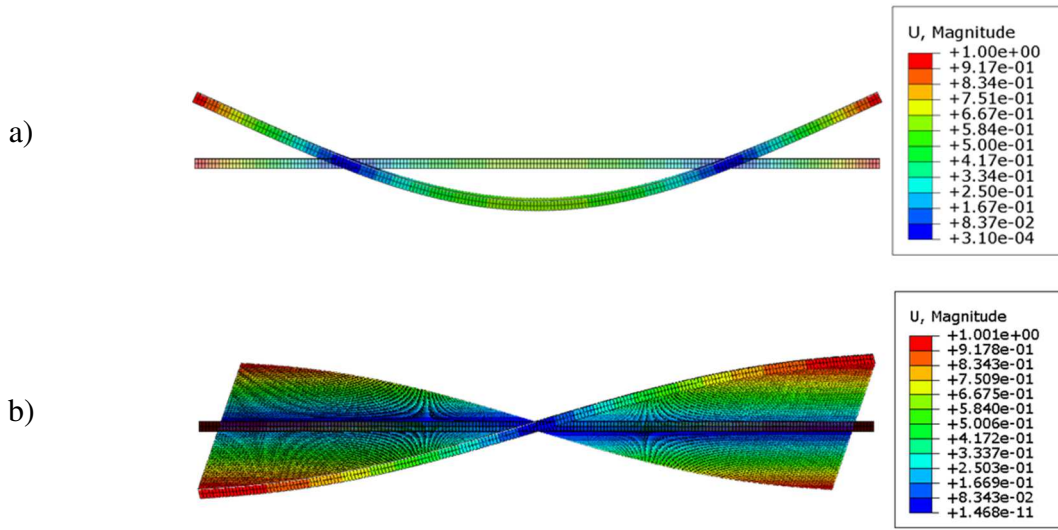


**Fig. 1.** Deformed beams at the fundamental harmonic mode: a) flexural vibrations, b) torsional vibrations. The colors indicate the vertical displacement (mm).

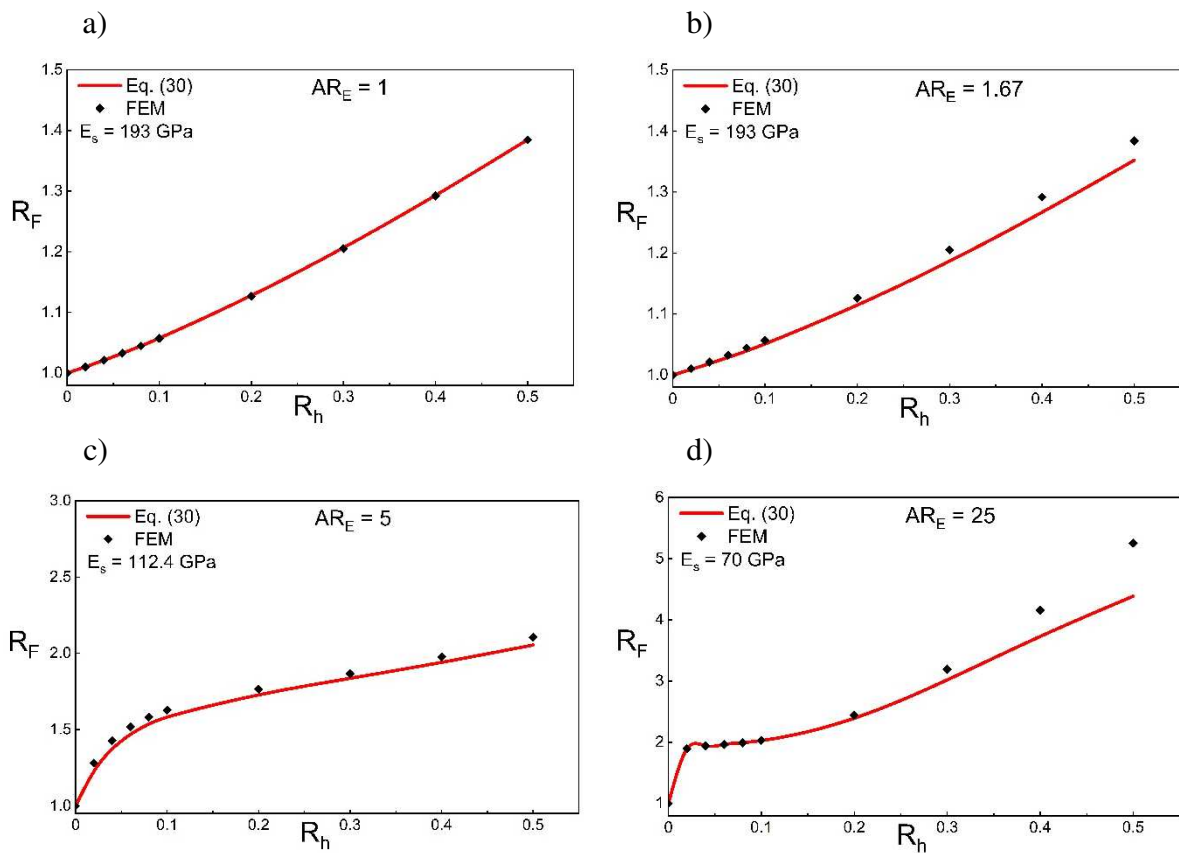


**Fig. 2.** Comparison between the developed analytical model and the numerical model: a)  $AR_E = 1$ , b)  $AR_E = 1.67$ , c)  $AR_E = 5$ , d)  $AR_E = 25$ .

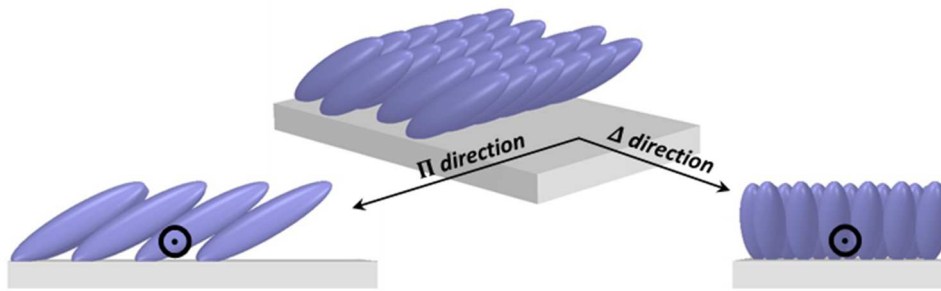


**Fig. 3.** Schematic illustration of  $\Delta$  and  $\Pi$  directions.

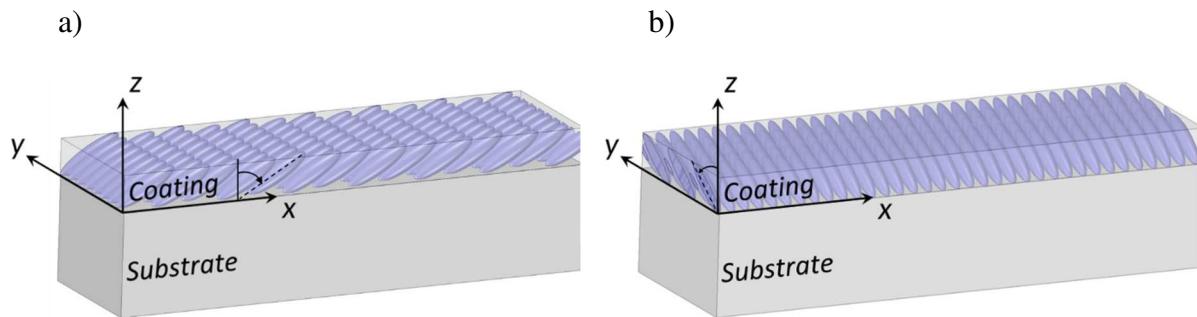


**Fig. 4.** Schematic illustration of the orientation of the columns in a film deposited towards: a) the longitudinal direction of the beam ( $\Delta \rightarrow X$ ) and b) the transverse direction of the beam ( $\Delta \rightarrow Y$ ).

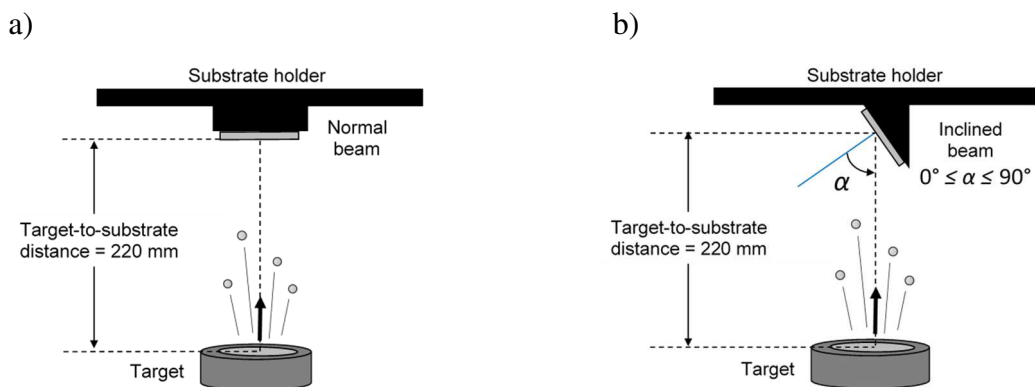


**Fig. 5.** Schematic illustration of PVD configurations in: a) conventional sputtering and b) GLAD sputtering.

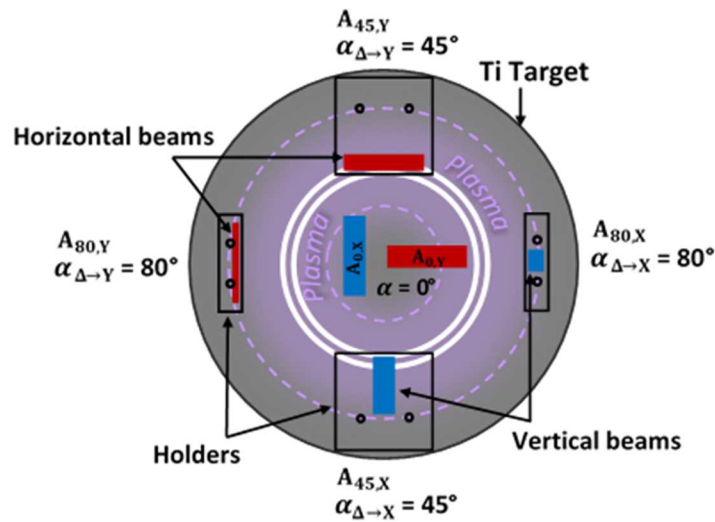


**Fig. 6.** Top-view configuration representing the Ti target with a projection of the holders and substrates positions. The samples in red correspond to the horizontal beams. The samples in blue correspond to the horizontal beams. (For interpretation of the references to color in this figure legend, the reader is referred to the Web version of this article).

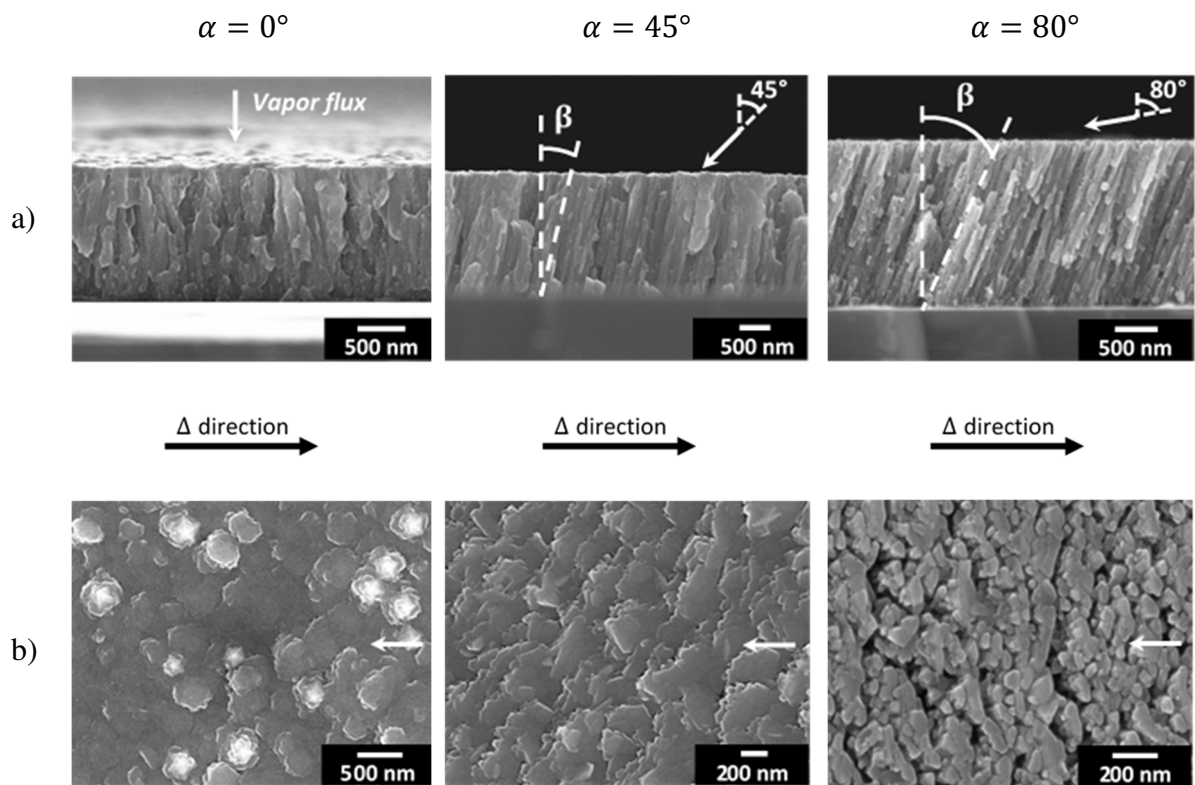


**Fig. 7.** Cross-section (a) and top view (b) SEM images of Ti films grown by glancing angle deposition at various glancing angles  $\alpha$  ( $0^\circ$ ,  $45^\circ$  and  $80^\circ$ ).

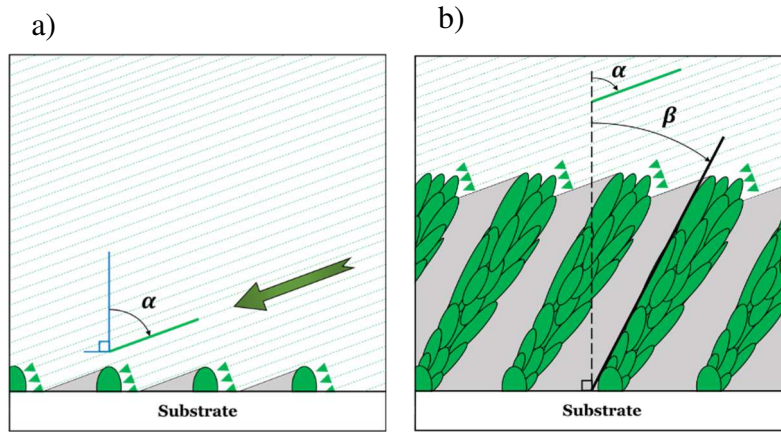


**Fig. 8.** A conceptual view of film growth in the GLAD process. a) The incident adatoms arriving at a glancing angle  $\alpha$  with respect to the surface normal. b) The adatoms are intercepted by growing nanocolumns, which form an angle  $\beta$  with respect to the surface normal. The grey areas are the shadowed regions created where no growth occurs.

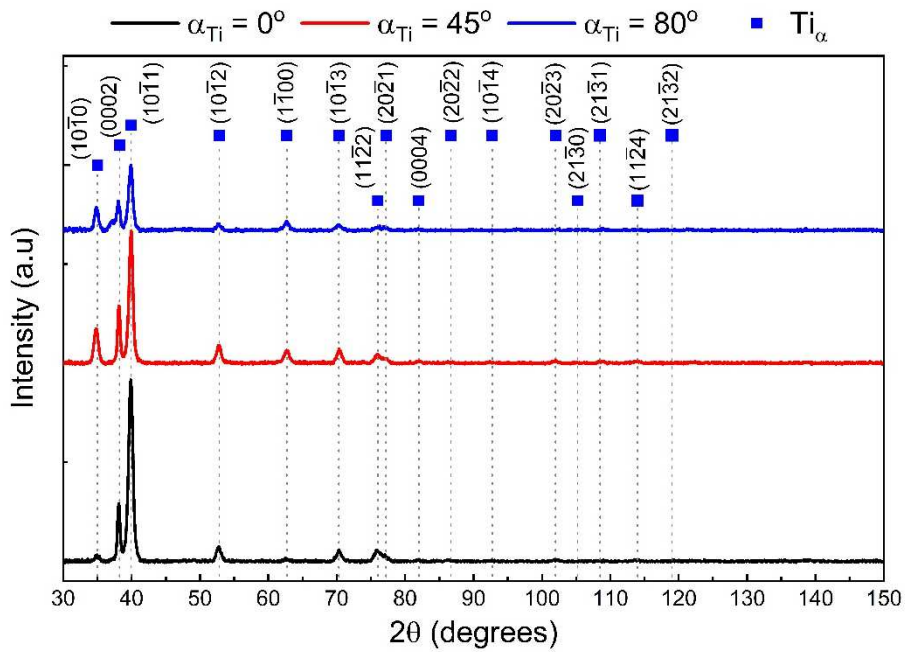


**Fig. 9.** Sum of the X-ray diffraction patterns of titanium films grown for the three values of the glancing angle  $\alpha$  ( $0^\circ$ ,  $45^\circ$  and  $80^\circ$ ).

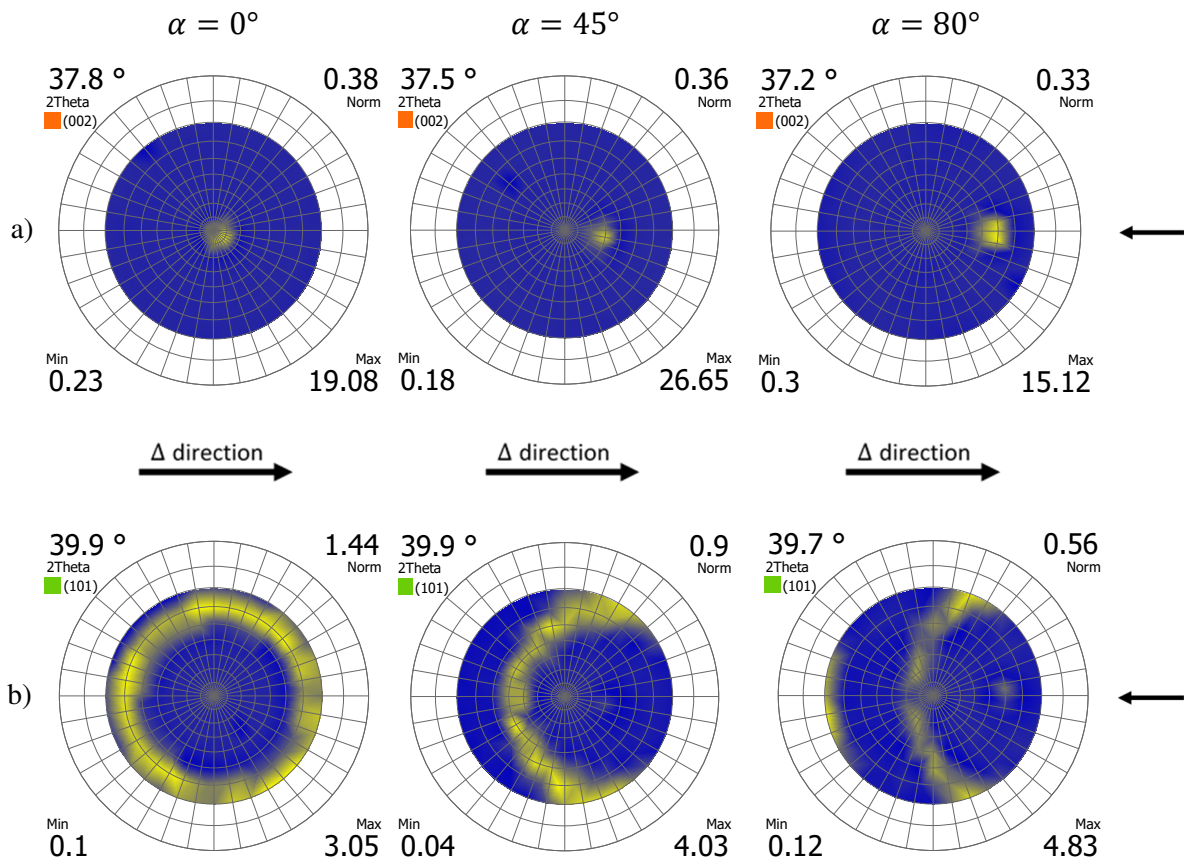


**Fig. 10.**  $\{0002\}$  (a) and  $\{10\bar{1}1\}$  (b) experimental pole figures of the  $Ti_\alpha$  phase by glancing angle deposition at various glancing angles  $\alpha$  ( $0^\circ$ ,  $45^\circ$  and  $80^\circ$ ). The pole figures are represented in stereographic projection and the arrows at the right of the figures show the vapor flux direction.

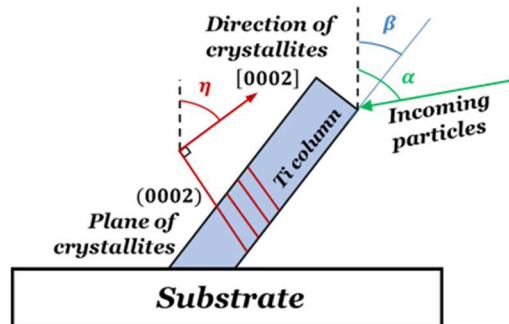


**Fig. 11.** Illustration of an obliquely deposited tilted Ti thin film with columnar growth ( $\beta$  angle), tilted fiber texture ( $\eta$  angle) and glancing angle  $\alpha$ .

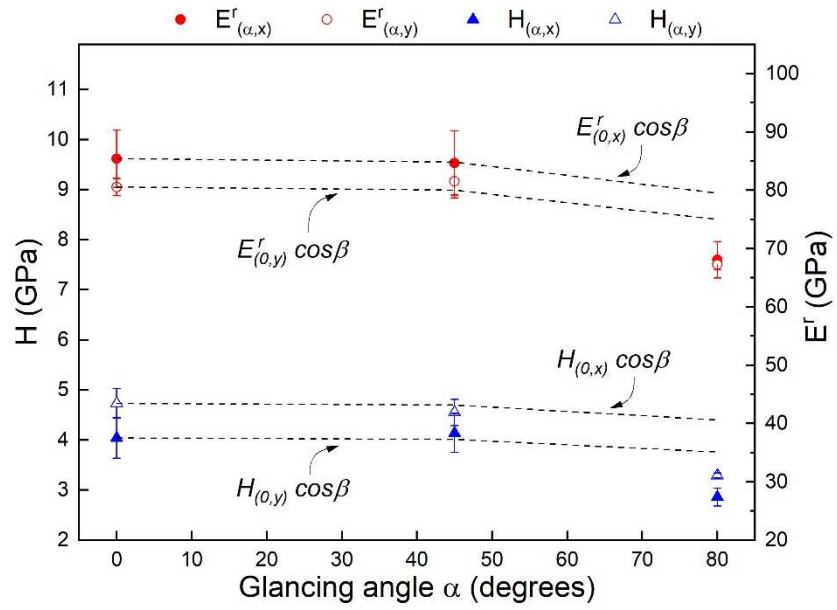


**Fig. 12.** Influence of the deposition glancing angle  $\alpha$  on the mean value of the hardness  $H_c$  and the reduced modulus  $E'_c$  of the titanium films measured by nanoindentation.

## List of Tables

**Table 1.**

The substrates and films properties with the measurement uncertainties.

Parameter	Symbol	Samples					
		$A_{0,X}$	$A_{0,Y}$	$A_{45,X}$	$A_{45,Y}$	$A_{80,X}$	$A_{80,Y}$
Deposition direction	$\Delta$	X-axis	Y-axis	X-axis	Y-axis	X-axis	Y-axis
Glancing angle ( $\pm 2^\circ$ )	$\alpha$	0	0	45	45	80	80
Columns tilt angle ( $\pm 2^\circ$ )	$\beta$	0	0	5	4	21	21
	$\beta_{cos}$	0	0	31	31	46	46
	$\beta_{tan}$	0	0	39	39	77	77
Fiber tilt angle ( $\pm 3^\circ$ )	$\eta$	7	6	30	29	46	43
Length ( <i>mm</i> )	$L$	$75.41 \pm 0.01$	$75.48 \pm 0.05$	$75.36 \pm 0.01$	$75.49 \pm 0.01$	$75.36 \pm 0.02$	$75.43 \pm 0.04$
Width ( <i>mm</i> )	$b$	$25.31 \pm 0.01$	$25.35 \pm 0.03$	$25.35 \pm 0.01$	$25.38 \pm 0.02$	$25.38 \pm 0.01$	$25.4 \pm 0.01$
Thickness	$h_s$ ( <i>mm</i> )	$1.003 \pm 0.001$	$0.975 \pm 0.001$	$1.016 \pm 0.002$	$0.986 \pm 0.001$	$1.039 \pm 0.002$	$0.969 \pm 0.002$
	$h_c$ ( $\mu m$ )	$1.461 \pm 0.032$	$1.380 \pm 0.032$	$2.063 \pm 0.067$	$1.592 \pm 0.056$	$1.997 \pm 0.057$	$1.187 \pm 0.059$
Mass ( $\pm 10^{-4}$ g)	$m_s$	4.7178	4.5745	4.7641	4.6217	4.8741	4.5663
	$m_c$	0.0119	0.0111	0.0155	0.0124	0.0129	0.0081
Density ( $kg/m^3$ )	$\rho_s$	$2464.44 \pm 2.66$	$2452.05 \pm 4.17$	$2454.53 \pm 4.94$	$2446.49 \pm 3.16$	$2452.71 \pm 4.86$	$2459.59 \pm 5.33$
	$\rho_c$	$4267.52 \pm 100.13$	$4203.72 \pm 104.73$	$3932.91 \pm 130.24$	$4065.35 \pm 146.75$	$3377.37 \pm 99.91$	$3561.69 \pm 182.43$

**Table 2.**

The IET measured quantities and the macroscopic elasticity constants of the glass substrates (assumed to be elastically isotropic) and the anisotropic Ti films at various deposition glancing angles.

Parameter	Symbol	Samples					
		$A_{0,X}$	$A_{0,Y}$	$A_{45,X}$	$A_{45,Y}$	$A_{80,X}$	$A_{80,Y}$
Frequencies before deposition ( $\pm 0.117$ Hz)	$F_s$	966.334	936.110	975.923	946.571	1000.010	936.616
	$T_s$	1792.796	1739.270	1810.487	1757.214	1852.695	1734.936
Frequencies after deposition ( $\pm 0.117$ Hz)	$F_t$	968.105	937.745	977.284	948.199	999.504	937.193
	$T_t$	1795.170	1741.480	1812.940	1759.310	1852.360	1735.380
Young's modulus (GPa) (IET)	$E_s$	$70.31 \pm 0.21$	$69.73 \pm 0.26$	$69.42 \pm 0.41$	$69.38 \pm 0.22$	$69.45 \pm 0.21$	$70.71 \pm 0.44$
	$E_\Delta$	$99.56 \pm 7.85$	-	$62.83 \pm 6.69$	-	$15.63 \pm 8.22$	-
	$E_\Pi$	-	$95.82 \pm 8.66$	-	$92.05 \pm 7.83$	-	$65.34 \pm 9.26$
	$E_X$	$98.88 \pm 5.34$	$96.47 \pm 5.88$	$68.23 \pm 3.95$	$87.08 \pm 5.48$	$19.44 \pm 3.89$	$57.32 \pm 6.87$
Shear modulus (GPa) (IET)	$G_s$	$28.341 \pm 0.084$	$28.2 \pm 0.09$	$28.112 \pm 0.164$	$28.078 \pm 0.086$	$28.131 \pm 0.081$	$28.559 \pm 0.175$
	$G_{\Pi Z}$	$33.83 \pm 1.46$	-	$27.75 \pm 1.27$	-	$11.24 \pm 0.98$	-
	$G_{\Delta Z}$	-	$33.27 \pm 1.52$	-	$29.65 \pm 1.55$	-	$17.89 \pm 1.76$
Poisson ratio (IET)	$\nu_s$	$0.24 \pm 0.005$	$0.236 \pm 0.006$	$0.235 \pm 0.01$	$0.236 \pm 0.005$	$0.234 \pm 0.005$	$0.238 \pm 0.01$
Anisotropic ratio	$AR_E$	$0.96 \pm 0.11$		$1.46 \pm 0.19$		$4.18 \pm 2.27$	
	$AR_G$	$0.98 \pm 0.06$		$1.07 \pm 0.07$		$1.59 \pm 0.21$	
Porosity (%)	(Eq. (44))	$5.17 \pm 2.23$	$6.58 \pm 2.33$	$12.60 \pm 2.9$	$9.66 \pm 3.26$	$24.95 \pm 2.22$	$20.85 \pm 4.05$
	ImageJ	$4.62 \pm 0.51$	$5.83 \pm 0.78$	$11.21 \pm 0.94$	$7.54 \pm 1.31$	$26.81 \pm 1.12$	$22.21 \pm 1.08$
Young's modulus (GPa) (Eq. (42))	$E^*$	$98.02 \pm 7.75$	$93.09 \pm 8.10$	$72.14 \pm 10.08$	$82.39 \pm 11.35$	$29.18 \pm 7.73$	$43.44 \pm 14.11$
Shear modulus (GPa) (Eq. (43))	$G^*$	$37.06 \pm 2.96$	$35.17 \pm 3.09$	$27.16 \pm 3.86$	$31.08 \pm 4.34$	$10.72 \pm 2.96$	$16.18 \pm 5.4$
Difference (GPa)	$E^{IET} - E^*$	1.54	2.73	9.31	9.66	13.55	21.9
	$G^{IET} - G^*$	3.23	1.9	0.59	1.43	0.52	1.71
Uncertainty (GPa)	$u(E)$	7.85	8.66	6.69	7.83	8.22	9.26
	$u(G)$	1.46	1.52	1.27	1.55	0.98	1.76

**Table 3.**

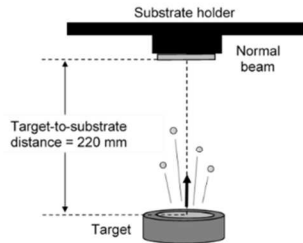
Summary of glass and titanium elasticity constants found in the literature.

Material		Young's modulus (GPa)	Shear modulus (GPa)	Poisson ratio	Reference
Glass	Bulk	69.84 – 70.07	29.43 – 29.51	0.187	[17]
		68.7 – 70.26	-	-	[18]
		-	30	0.175	[20]
Ti	Bulk	115 – 116	-	0.31 – 0.32	[45,47]
		97 – 112	-	-	[18]
Ti	Thin film	61 – 113	-	-	[45]
		90 – 100	-	-	[46]
		102.6 – 110	-	0.31	[47]
		115.7	-	0.321	[48]

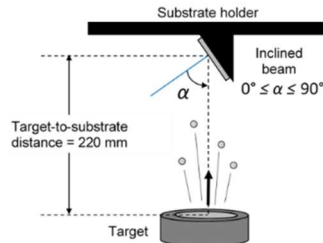
# Graphical Abstract

## Magnetron Sputtering

### Conventional Deposition

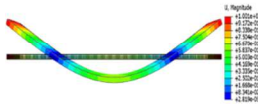


### Glancing Angle Deposition

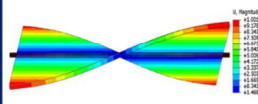


### Impulse Excitation Technique

#### Flexural Frequencies



#### Torsional Frequencies



### Effect of the glancing angle $\alpha$

#### Film Microstructure

Morphology: Columns Tilt Angle  
Phase:  $Ti_{\alpha}$ -hcp  
Texture: Fiber Tilt Angle  
Porosity

#### Mechanical Properties

Hardness  
Reduced Modulus

### Mechanical Model for Anisotropic Thin Films

Before deposition for substrate

After deposition for the Composite = Substrate + Film

Inverse Method

### Surface Anisotropy

### Elasticity Constants of Anisotropic Film

$E_{\Delta}$   
 $E_{\Pi}$   
 $G_{\Pi Z}$   
 $G_{\Delta Z}$

#### Macroscopic Scale

